# An integrated approach for the analysis and control of grid connected energy storage systems

Charalampos Patsios[a,*], Billy Wu[b,c], Efstratios Chatzinikolaou[d], Daniel J. Rogers[d], Neal Wade[a], Nigel P. Brandon[b], Phil Taylor[a]

[a] School of Electrical and Electronic Engineering, Newcastle University, UK
[b] Department of Earth Science and Engineering, Imperial College London, UK
[c] Dyson School of Design Engineering, Imperial College London, UK
[d] School of Engineering, Cardiff University, UK

ABSTRACT

This paper presents an integrated modelling methodology which includes reduced-order models of a lithium ion battery and a power electronic converter, connected to a 35-bus distribution network model. The literature contains many examples of isolated modelling of individual energy storage mediums, power electronic interfaces and control algorithms for energy storage. However, when assessing the performance of a complete energy storage system, the interaction between components gives rise to a range of phenomena that are difficult to quantify if studied in isolation. This paper proposes an integrated electro–thermo–chemical modelling methodology that seeks to address this problem directly by integrating reduced-order models of battery cell chemistry, power electronic circuits and grid operation into a computationally efficient framework. The framework is capable of simulation speeds over 100 times faster than real-time and captures phenomena typically not observed in simpler battery and power converter models or non-integrated frameworks. All simulations are performed using real system load profiles recorded in the United Kingdom. To illustrate the advantages inherent in such a modelling approach, two specific interconnected effects are investigated: the effect of the choice of battery float state-of-charge on overall system efficiency and the rate of battery degradation (capacity/power fade). Higher state-of-charge operation offers improved efficiency due to lower polarisation losses of the battery and lower losses in the converter, however, an increase in the rate of battery degradation is observed due to the accelerated growth of the solid-electrolyte interphase layer. We demonstrate that grid control objectives can be met in several different ways, but that the choices made can result in a substantial improvement in system roundtrip efficiency, with up to a 43% reduction in losses, or reduction in battery degradation by a factor of two, depending on battery system use case.

## 1. Introduction

The challenge of integrating large amounts of intermittent renewable generation on electrical grids calls for smarter management of electrical networks and brings with it new business opportunities. The United Kingdom (UK) has signed up to the European Union renewables energy directive which includes aims of having 15% renewable energy on the grid by 2020, a 7-fold increase on the 2008 level [1–4], and is further committed to reduce its greenhouse gas emissions so that by 2050 they are at least 80% below 1990 levels [4]. Electrical energy storage (EES) has

been identified as one of the ways of supporting this low carbon transition [5]. Facilitating EES has been considered an essential component of future UK smart grids [6]. Although a number of trials are already active in the UK [5–8], ranging from domestic community-scale devices to industrial utility-scale systems with power and energy capacities from some kW and kWh, respectively up to a few MW and MWh, there remain many technical and economic questions regarding the feasibility of large scale EES systems.

A grid-scale energy storage system is composed of three main components: the energy storage medium itself (e.g. lithium-ion batteries), a power electronic interface that connects the storage medium to the grid, and a high-level control algorithm that chooses how to operate the system based on measurements internal (e.g. state-of-charge) and external to the system (e.g. busbar voltage). At

* Corresponding author.
  E-mail address: haris.patsios@newcastle.ac.uk (C. Patsios).

present, controllers that are designed to achieve a grid control objective do not account for the detailed operation of the power electronic grid interface or the electrochemical performance of the batteries [9–11]. This level of detail is often omitted to improve simulation time as grid studies usually span several hours to months. However, this simplification can result in inaccurate predictions due to the non-linear nature of electrochemical devices, highlighting the need for models which retain the physical phenomena of relevance in this area. In this paper, we propose an integrated modelling approach. We implement a physics-based battery and a power converter model with sufficient level of detail to accurately account for energy losses, and to track one form of battery degradation (solid-electrolyte interphase (SEI) layer growth). This battery energy storage system (BESS) model is coupled with a grid model based on a typical network case in the UK.

The academic literature concerning the modelling of each sub-system is vast and covers a multitude of applications. Typically, power converter operation is modelled for times ranging from microseconds to a few tens of seconds [12,13], battery system operation from milliseconds to tens of minutes [14–17] and electrical networks from seconds to days [18–21]. Research involving the modelling of each system rarely takes an integrated approach, as the scope and field of application varies widely. When ESSs are employed in grid-connected applications, simplifications are usually made in the modelling of batteries, for example when the simulation time window is extended (e.g. in analysis of cost-effectiveness [18–21]), or the examined timescale is short due to a focus on the design of a proposed control algorithm [22,23]. There are examples of a more holistic approach involving different timescales, but this is often made in a non-integrated manner such that different models are used to simulate each timescale [24].

Fig. 1 summarises the various effects of the different grid-connected devices and the timescales over which they occur. The area highlighted in green covers the timescales addressed within the developed integrated modelling framework. The proposed benefits stemming from this approach are:

- To allow for a precise and on-line mapping of asset characteristics and associated operating costs focusing on the edges of nominal limits.
- To assist in efforts towards a more cost-effective sizing of grid-connected energy storage system applications and thus reduction of initial costs.
- To lead to a more efficient and cost-effective operation maximizing benefits of BESS operation.
- To allow for the development and testing of novel control architectures in a more realistic and detailed environment.
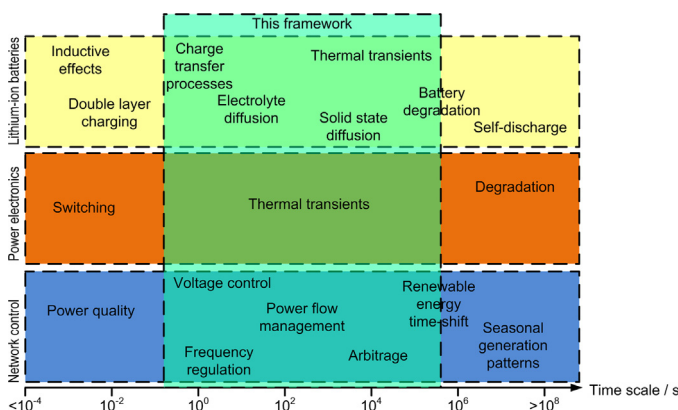


**Fig. 1.** Relative time scales and effects for different areas of interest. The area highlighted in green covers the timescales addressed by the integrated modelling framework presented in this paper.

- To facilitate the incorporation of the model in real-time simulation platforms.

## 2. Methodology

Fig. 2 shows a block diagram of the integrated model and details of individual blocks. Extended descriptions of the individual systems are given in the following sections. Overall, the lithium-ion battery model receives battery current, $I_b$, from the power converter model and outputs battery voltage, $V_b$, state of charge, SoC, and battery temperature, $T_{bat}$, to the network model which can be used for control purposes. A degradation mechanism (SEI layer growth) is also implemented in the battery model; capacity loss data, $C_{loss}$, in Ah can thus be used for realising cost functions that take into account battery life decline, however a full degradation model is beyond the scope of this paper. The converter model receives active and reactive power set-points, $P$ and $Q$, respectively from the network control algorithm as well as the voltage at the point of common coupling (PCC), $V_{PCC,RMS}$ and calculates the respective current, $I_{PCC,RMS}$, and phase angle, used for calculations in the grid model. Power converter efficiency and the junction temperature of the Insulated gate bipolar transistors (IGBT) s, $T_j$, are calculated. Whole system energy losses, $E_{loss}$, are also calculated by integrating power converter losses, $P_{loss,avg}$, and battery power, $P_{bat}$. Battery round trip energy efficiency is calculated over a cycle that begins and ends at the same SoC. MATLAB/Simulink® is used for implementing this model. The network model is designed using the Simpowersystems™ library while the battery and converter models are implemented as embedded MATLAB® functions.

### 2.1. Lithium-ion battery model

The equations which govern the operation of a lithium-ion battery can be solved in varying degrees of complexity; 3D [25,26], 2D [27,28], 1D [29,30] and 0D [31]. In the case of the 0D model, this is known as the single particle model (SPM), which is diagrammatically shown in Fig. 2b and has been adopted in this work. This has advantages in terms of low computational cost, however it is typically only valid up to approximately 2C (1C being the current required to discharge the cell in 1 h and thus 2C being twice this value) operation, though often load balancing services on grids are below this rate thus enabling its use. Here the concentration gradients induced in the electrolyte phase are assumed to be constant.

There are many degradation mechanisms relevant to lithium-ion batteries. These can include: the growth of the SEI layer, mechanical fracture of the electrodes due to volume changes, electrolyte decomposition, cathode dissolution, dendrite formation, lithium plating and many others [32]. This modelling work includes the effect of SEI layer growth, a degradation effect often cited as a critical factor [33] causing both power fade through increase in cell resistance and capacity fade through loss of active material. Whilst others exist, it is beyond the scope of this paper to present a battery model covering all degradation modes.

The battery chemistry used in this study is based on Kokam 4.8 Ah lithium–polymer cells with an operating voltage window of 4.2–2.7 V. This uses a graphite anode and metal oxide cathode, common to many lithium-ion battery chemistries. This single cell is then scaled to grid scale by increasing the number of cells in series and parallel. Depending on the battery chemistry used, the resistance over the whole SoC range and at different temperatures will not be constant due to variations in the charge transfer resistance of the electrodes and diffusion processes [34]. This is demonstrated in Fig. 3 which shows measured resistance values
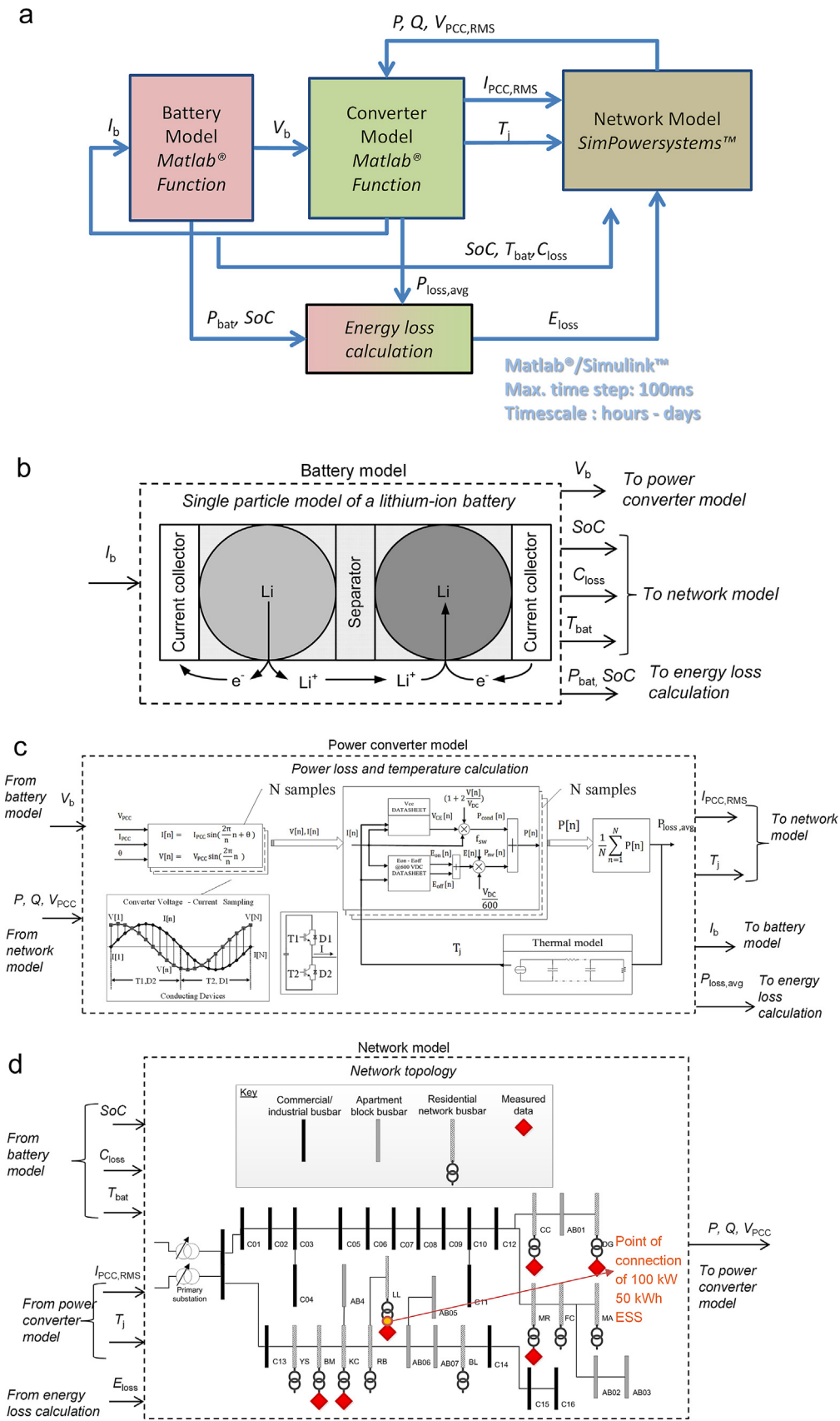
**Fig. 2.** Block diagram of the proposed integrated model and details of individual blocks (a) whole system (b) Single particle model of a lithium-ion battery showing schematic of the domains of interest (c) power converter model and loss calculation procedure (d) network model showing MV network topology and measurement points at the LV secondary substations.

fitted from the equivalent circuit inset shown in Fig. 3, obtained from electrochemical impedance spectroscopy (EIS) measurements. Here it can be seen that at SoCs below 40%, both the charge transfer resistance and the diffusion resistance increase significantly. Operating the energy storage system within this range therefore reduces the round trip efficiency of the system and also increases the heat generation from the battery, which if not thermally managed can cause accelerated battery degradation.

An important interaction of the battery chemistry with the power electronics is that the battery voltage varies significantly with SoC. Fig. 4 shows how the cell voltage of a battery varies with SoC when under galvanostatic operating mode with a current of 2.4 A (0.5C). Thus, selecting a suitable SoC range and designing the electronics around that voltage range becomes an important optimisation step when designing for grid storage applications.

Here it can be seen that, when the SoC falls below 20% it becomes more difficult to operate the device due to the large voltage swing and the accompanying increase in impedance, which impacts both round trip efficiency and heat generation.

### 2.1.1. Battery model

The battery SPM accounts for non-linear electrochemical performance by treating each electrode as equivalent to a single sphere, modelling solid-state lithium diffusion in each electrode to define the individual electrode potentials which are then coupled to a stoichiometry-potential function and the Butler–Volmer equation to give overall cell performance. Here electrolyte concentration gradients are neglected due to the assumption of low (<2C) discharge/charge rates. Heat generation in the battery is also reduced to only account for the reaction heats and electronic Ohmic heating for simplification. In the majority of cases, the entropic heat is much smaller in magnitude than the other heat generation terms and can be neglected [29]. Also, since there are no lithium-ion electrolyte concentration gradients, the ionic heat term does not need to be considered. Furthermore, the heat generated from the solid state lithium diffusion was found to be significantly smaller than that of the electronic Ohmic and reaction heats, and thus was neglected [29]. The temperature, modelled as a lumped capacitance model, is then coupled to the performance of the cell via an Arrhenius rate law equation. The rate of degradation was fitted to the model based on the physical parameters provided by Ramadass et al. [33] and fitting of the exchange current density of the side reaction to the capacity loss presented by Wu et al. [36] who used the same cells. The modelling approach for the SPM is based on the work by Chaturvedi and Klein [35] and Ramadass
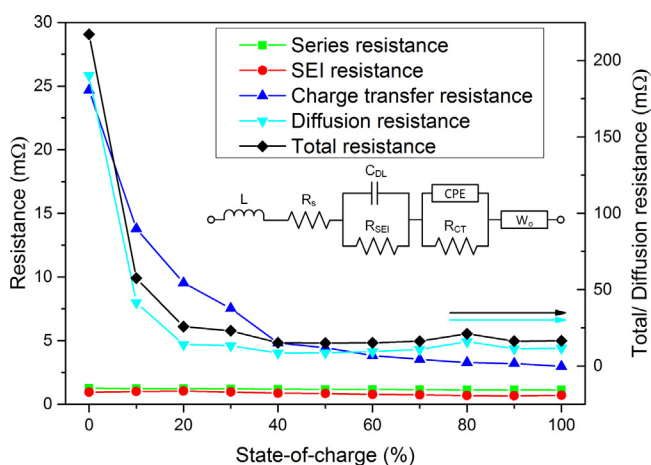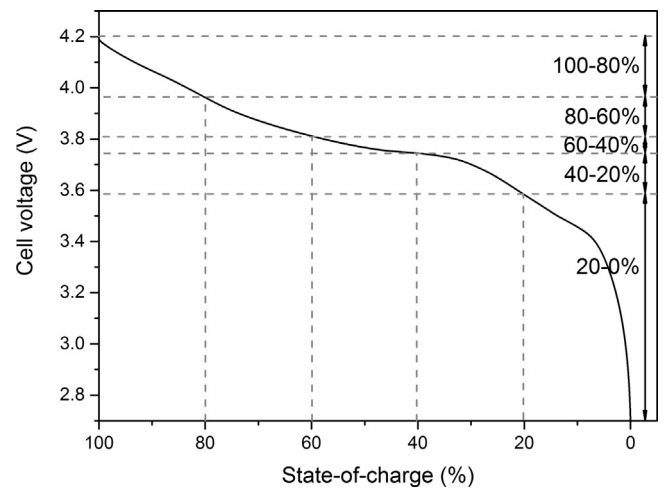
Fig. 4. Measured cell voltage as a function of SoC for a 4.8 Ah Kokam lithium-ion battery.

et al. [33] and readers are directed to these papers for the details of the governing equations which were adopted in this work unless otherwise stated. The parameters used in the model are shown in Appendix A and the fitted electrode potential curves are shown in Fig. 15.

The battery model was implemented as a MATLAB® s-function, employing Finite Difference Methods (FDM) to solve the differential equations. This function was incorporated into Simulink®, where the block adopts the battery states from the previous time step and calculates the next time step based on the governing equations.

### 2.1.2. Model validation

Model validation was done by testing the cells under different discharge rates using a Maccor 4300 battery tester in a 4-electrode configuration and k-type thermocouples attached to the centre of the cell with Kapton tape. The comparison between the model and experimental results are shown in Fig. 5 for both the voltage and temperature response.

### 2.2. Converter model

The most popular topologies used to interface a BESS with the AC network are single stage and two stage converter topologies. In a single stage topology, the battery pack is connected directly to the DC link of a voltage source converter. Due to the varying battery voltage it is not possible to optimise the inverter design for a specific DC-link voltage, resulting in an 'oversized' DC to AC stage. In the two stage topology, a DC to DC conversion stage is used in order to boost the battery voltage and regulate the DC-link voltage so that the DC to AC stage can be optimised [37]. In this study, the two stage topology presented in Fig. 6 is used as it allows greater variation in battery voltage, and hence more complete charge extraction, without compromising the efficiency of the system [38]. Table 1 summarizes the parameter values of the two stage topology shown in Fig. 6.

The efficiency of the power converter is strongly dependent on the conduction and switching losses of the internal semiconductor devices and to a lesser degree on the losses in the passive filter components (filter inductors and capacitors and the DC link capacitor) [39]. One method of calculating switching and conduction losses is to use a transient simulation using a very short time step simulation to capture every switching edge (this is referred to as the 'detailed model'). This typically requires a time step in the order of 1 μs in order to maintain accuracy [40]. The obvious
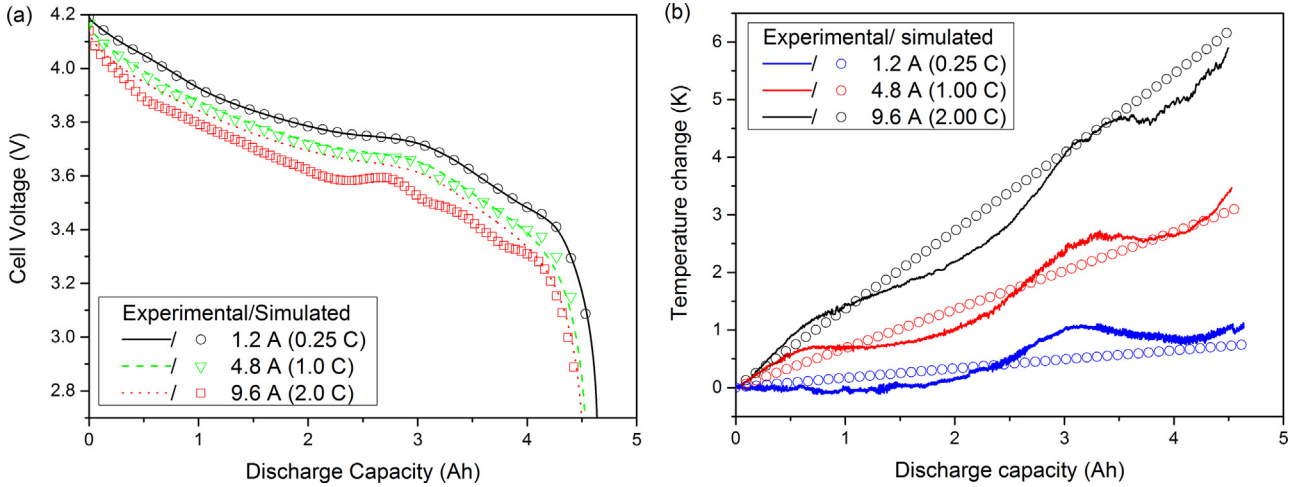
Fig. 3. Fitted EIS spectra from measurements of a 4.8 Ah Kokam lithium–polymer battery at different SoCs, with equivalent circuit inset.

**Fig. 5.** Measured and simulated (a) voltage and (b) temperature responses of a 4.8 Ah Kokam lithium–polymer cell.

drawback of this method is that it is inherently very computationally expensive. This work targets simulation speeds faster than real time and so an alternative method of converter loss simulation has been developed. This method emphasises close agreement with the detailed simulation approach in steady state operation.

The proposed method, referred to here as the 'average model', is based on semiconductor datasheet information [41] coupled to a piecewise linear approximation of a single 50 Hz fundamental period of the voltages and currents occurring in one leg of a three-phase bridge. As balanced three-phase waveforms are assumed during simulation, power losses need to be calculated only for a pair of semiconductors. The voltage ($V[n]$) and current ($I[n]$) samples are used to calculate the conduction and switching losses according as

$$P_{cond}[n] = I[n]V_{CE}[n]D[n] \tag{1}$$

$$P_{SW}[n] = f_{SW}(E_{on}[n] + E_{off}[n]) \tag{2}$$

where $V_{CE}[n]$ is the voltage across the semiconductor device, $D[n] = \left(1 + 2\frac{V[n]}{V_{DC}}\right)$ the modulation ratio for a specific sample $n$, $f_{SW}$ the switching frequency and $E_{on}[n], E_{off}[n]$ the switch-on and switch-off energy losses, respectively.

The sum of these losses represents the total power losses of the converter for each sample and is then used to calculate the average power losses for a fundamental period of 50 Hz. The junction temperature of the semiconductors devices is estimated using a Cauer thermal model as in [42]. The power loss calculation for the IGBT (T1) using the average model is presented in Fig. 2c the same procedure applies for the diode (D1) except that only reverse recovery switching losses are considered, i.e. $E_{on}[n] \equiv 0$ [43].

The average model also takes into account power losses occurring in the LC filter of the DC/DC converter, the LCL filter at the grid side of the AC/DC converter and the DC link capacitor.

These losses are described in Eqs. (3)–(5) with regard to Fig. 6.

$$P_{CDC} = R_{CDC}(2\pi f_{SW}C_{DC}\Delta V_{DC})^2 \tag{3}$$

$$P_{LG} = 3I_G^2(R_{LG2} + R_{LG2}) \tag{4}$$

$$P_{LB} = I_B^2 R_{LB} \tag{5}$$

where $R_{CDC}$ is the equivalent series resistance of the DC link capacitor, $\Delta V_{DC}$ the voltage ripple at the DC link, $R_{LG1}, R_{LG2}, R_{LB}$ the DC resistance of the inductors $L_{G1}, L_{G2}, L_B$, respectively. The model also incorporates transformer no load losses based on datasheet information [44]. The accuracy of the average model is calculated based on the mean absolute percentage error ($M$) as given in Eq. (6) and depends on the number of samples $N$ used in the calculations.

$$M = \frac{100}{K}\sum_{t=1}^{K}\left|\frac{P_{det}[t] - P_{avg}[t]}{P_{det}[t]}\right|\% \tag{6}$$

where $K$ is the total number of average losses samples, $P_{det}[t]$ the average power losses based on the detailed model and $P_{avg}[t]$ the average power losses based on the average model. Fig. 7 demonstrates the relation between the absolute error and number of samples used in the calculations. A number of 20 samples per cycle (one period of the fundamental grid frequency) was observed to give good agreement with the detailed model with low computational effort and so was chosen for use in the rest of the work. Transient responses of the detailed and average models are shown in Fig. 8.

The detailed model requires approximately 300,000 steps for one second of simulation time whereas the average model requires only 52 steps. During each step power losses are calculated using a predefined number of samples, in this case 20, resulting in a mean absolute percentage error of 3.6%. (Fig. 7).
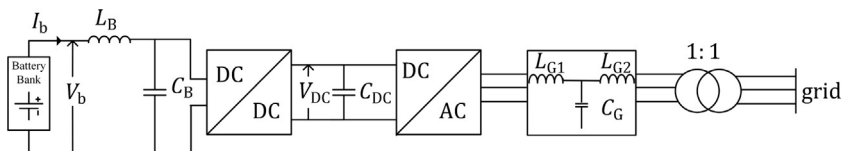


**Fig. 6.** Two stage topology comprised of battery bank, DC–DC and DC–AC conversion stages.

## 2.3. Network model and control algorithm

The section of network used to test the integrated model is based on a real low voltage (LV) network in the UK [45]. The network is connected to the medium voltage (MV) network through two 11 kV feeders and ultimately to the 33 kV network through a primary substation. Fig. 2d shows the network configuration. The network has a combination of commercial/small industrial customers and residential LV networks. The latter comprises both loads and PV systems.

A conceptual future scenario is examined to serve as a trial for the proposed integrated modelling approach: A 100 kW 50 kWh BESS is assumed to be connected directly to the secondary substation, as shown in Fig. 2d, rated at 315 kVA. The substation transformer is currently serving 5 feeders with a total of 208 load customers and 6 PV installations. At present loading conditions, the thermal limits of the transformer are not exceeded, however, the possibility exists that loading will be increased in the future such that network reinforcement would be required. In such a case, the BESS could serve as a means to flatten the high evening load peaks and reduce the transformer loading below the thermal thresholds while also providing a set of ancillary services.

For the purposes of this study, four measured power profiles—one for spring, summer, autumn and winter—comprising of aggregated load demand and PV generation were scaled from 4 to 8 times depending on the load case examined, so that the transformer's rated power is exceeded during the evening periods. One or more BESSs of the size considered could be connected directly at the secondary transformer, or positioned deeper inside the feeder, and be operated such that the transformer is kept within its thermal limits at all times through appropriate control (storing energy during the day and releasing it during the evening). The 24 h power profiles considered are shown in Fig. 9. The power profiles shown have originated from daily measurements taken throughout the year at the 6 secondary substations marked with a red rhombus in Fig. 2d. Measured data with 1 min resolution was made available by the distribution network operator (DNO). The data was recorded between November 2011 and March 2013 using KelVAtek data monitors/smart fuses [45]. Data includes phase currents, voltages, active and reactive power flows. Although Section 2.4 presents results referring only to the Autumn load, results for the rest of the load cases of Fig. 9 have been recorded but are not shown in this paper since the general findings are applicable in each case.

The grid model is implemented using the SimPowerSystems™ library in Simulink®. The model incorporates the battery and power converter models packaged as s-functions. The solver is the ode23t (an implementation of the trapezoidal rule using a free
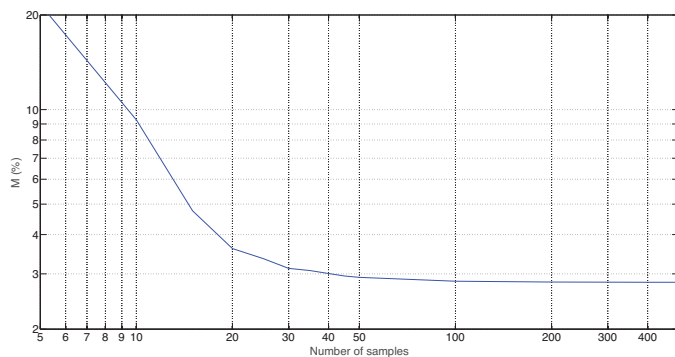
interpolant). Using a desktop computer system running on an Intel® Core™ i5-4670CPU at 3.4 GHz with 8 GB RAM the model runs approximately 100 times faster than real time. The BESS connection to the grid is implemented using current sources responding to active and reactive power set points. Power set points along with the voltage at the PCC are passed on to the converter model that calculates battery current and outputs the latter to the battery model which calculates battery parameters e.g. SoC, temperature, voltage and capacity losses.

Simulation of the electrical part is performed in phasor mode which provides fast simulation but limits the solution to one particular frequency. A full transient simulation is not required in this model because the BESS system control algorithm operates at timescales greater than 1 s. A grid modelling framework based on a sequential load-flow solution method was also considered but rejected. The minimum time step required by the battery model is 100 ms which implies a minimum of 864,000 load flows for simulating a single day using a closed-loop coupled model. This would also result in impractical simulation speed. Furthermore sequential load flows would eliminate any effects related to electrical transients and thus restrict system studies to steady-state analysis.

## 2.4. BESS control algorithm

The control algorithm's primary function is to follow the transformer load and respond by flattening it when this exceeds 300 kW by discharging the battery. The algorithm issues power commands that equal the difference between the load and the 300 kW threshold. The algorithm also accounts for the SoC and current limitations imposed by battery technology constraints when operating close to the SoC extremes; these are calculated online in the battery model and aim to maintain individual cell voltage between the 2.7–4.2 V limits.

The BESS will normally float at a pre-selected SoC. It will be allowed to charge, either prior to the evening peak or during the evening, by drawing power but ensuring the transformer 300 kW threshold is not exceeded. Achieving the target of flattening the transformer evening load will depend primarily on the available battery energy i.e. battery SoC. Depending on the load profile there are several hours during the day when the battery will be "idle" i.e. it will not charge or discharge and its SoC will float at a given set point. Available energy will also depend on the SoC upper and lower limits. In the various cases examined in this paper we will be simulating battery operation at different floating SoC and different SoC limits as these relate to battery degradation and overall system efficiency.

Fig. 10 displays the typical operation of the BESS. The BESS is set to float at 30% SoC. Shortly after noon the BESS will charge in order to be in a position to accommodate the evening peak. This operation is controlled so that the 300 kW transformer limit is not exceeded. The same applies for the BESS's nominal power and battery current constraints that depend on the operating battery SoC. The BESS will respond during the evening to flatten the transformer load and will be allowed to recharge if the SoC falls below 30%. The battery may recharge to higher SoCs during the evening if the algorithm is set to allow for this operation.

## 3. Results and discussion

Using the proposed integrated modelling approach, the system is simulated for an equivalent time window of 24 h. The Autumn load profile was chosen in this study as it is relatively higher and has a greater variability than the other seasons. It is thus anticipated that the BESS will reach its nominal power in

**Fig. 7.** Mean absolute percentage error between power losses calculation using the detailed converter model and power losses calculation using the proposed average model. The error is presented as a function of the number of voltage and current samples used in the average model calculations.
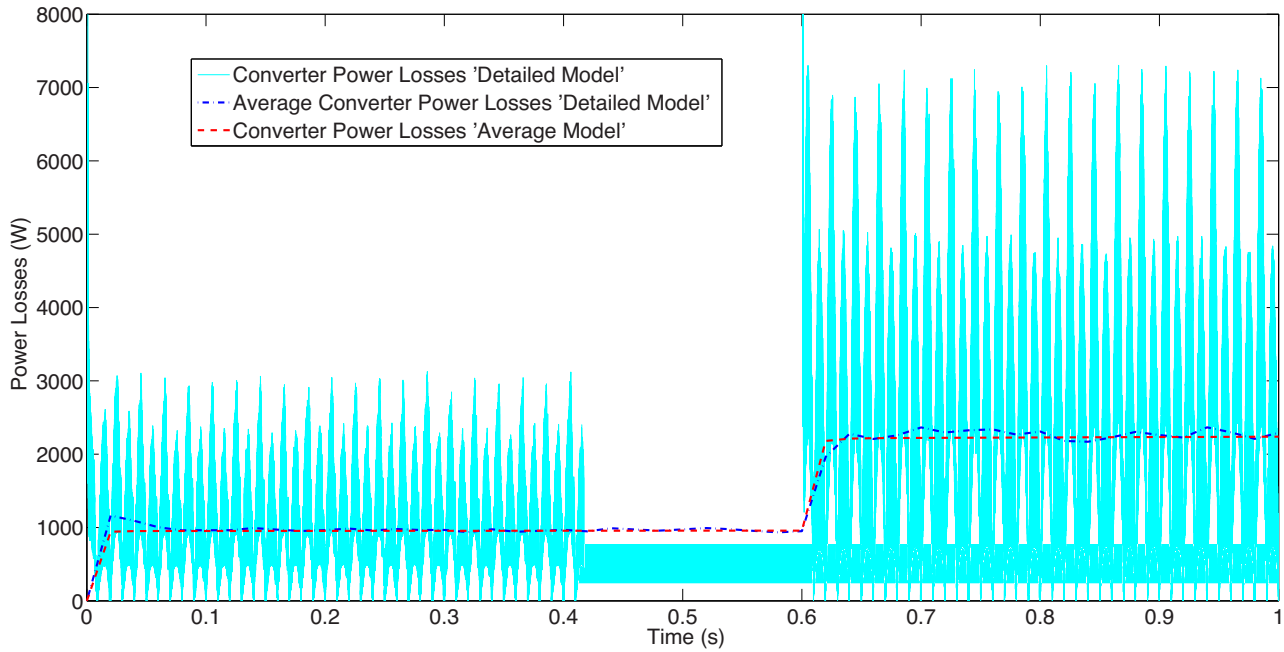
**Fig. 8.** Comparison between models for a step in converter active power from 0.5–1 p.u. at $t = 0.6$ s.

**Table 1**
Parameter values of the two stage topology.

| Parameter | Symbol | Value |
|---|---|---|
| Nominal DC link voltage | $V_{DC}$ | 700 V |
| Battery voltage range | $V_B$ | 405–630 V |
| Boost converter inductance | $L_B$ | 0.3 mH |
| Boost converter capacitance | $C_B$ | 10 μF |
| DC link capacitance | $C_{DC}$ | 3 mF |
| Grid filter inductance 1 | $L_{G1}$ | 0.6 mH |
| Grid filter inductance 2 | $L_{G2}$ | 15 μH |
| Grid filter capacitance | $C_G$ | 0.1 mF |

numerous instances and also operate near the SoC limits. The BESS is controlled using the control method described in the Section 2.3 in order to flatten the evening peak. Fig. 11 shows BESS operation for two different combinations of floating SoC, and SoC limits:

a Floating SoC 100%, maximum SoC 100%, minimum SoC 20%.
b Floating SoC 30%, maximum SoC 80%, minimum SoC 0%.

For these two combinations Fig. 11 shows the power flowing through the transformer, the BESS power, SoC, battery capacity loss and energy absorbed and released during the operation of the BESS. As can be seen in Fig. 11d, capacity loss varies significantly depending on the floating SoC, with lower SoCs resulting in lower degradation due to the higher anode potential and thus lower rate of SEI layer growth. Fig. 11e shows the energy absorbed and released by the battery system during charge and discharge respectively, starting at a value of 0 kWh. Charging increases this value and discharging reduces it. In both cases the cycle ends at the same SoC as the initial one i.e. 100% and 30%, respectively. The difference between the starting (0 kWh) and ending energy values, $\Delta E_{ESS}$, shown in the figure is measured in kWh and is calculated by integrating the power absorbed and released during the operation of the BESS. It will thus equal the roundtrip energy losses for the 24 h cycle. Fig. 11e shows a difference in these losses. The resulting

$\Delta E_{ESS}$ of 14.58 kWh and 14.17 kWh for the two cases of Fig. 11e signify a 93.27% and 93.56% roundtrip efficiency respectively. The above remarks suggest that although the energy delivered for these two cases is the same under the same power i.e. the effect on the service to the grid will be the same, the effect on the battery life and the overall energy efficiency of the system can be different.

A closer examination of the energy losses is undertaken for combination (a). The energy absorbed and released during the operation of the BESS is depicted in Fig. 12a for the whole system and the battery pack separately. These are split in the figure to total energy losses of the BESS and losses of the battery, i.e. $\Delta E_{ESS}$ and $\Delta E_{BAT}$, respectively. The energy dissipated in the batteries through internal irreversible losses is equal to 33.4% of the total losses. This indicates that the main contributor of losses in the BESS is the battery interface that consists of the power converter and transformer. Fig. 12b shows the dependency of the battery round trip efficiency (subsequently referred to as battery efficiency) on the change in SoC ($\Delta$SoC). Battery efficiency is measured for a cycle during which the battery is discharged from a predefined SoC set point and charged back to this point.

According to Fig. 12b (cycle a, b and d), battery efficiency decreases as the $\Delta$SoC is increased for cycles with equal SoC set points highlighting the influence of the SoC-impedance relationship and the decreasing cell voltage (resulting in increased losses for equal power requirements). In the case of cycles with similar $\Delta$SoC (cycle b and d), efficiency is higher in the cycles with the highest SoC set points, again highlighting the importance of capturing the SoC-impedance relationships. The decrease in efficiency when the battery is operated for higher $\Delta$SoC is thus underlined by the simulation shown in Fig. 12b where a maximum difference in battery losses of approximately 43% was recorded between the points examined. It should be highlighted that Fig 12b shows the magnitude of the efficiency changes based on a real world load cycle and thus absolute magnitude changes will vary based on system configuration and load cycle but the intention of the example is to highlight the importance of capturing relative effects and their effect on efficiency.

A series of simulations was then undertaken to study the effects of different floating SoC and SoC limits on battery degradation and
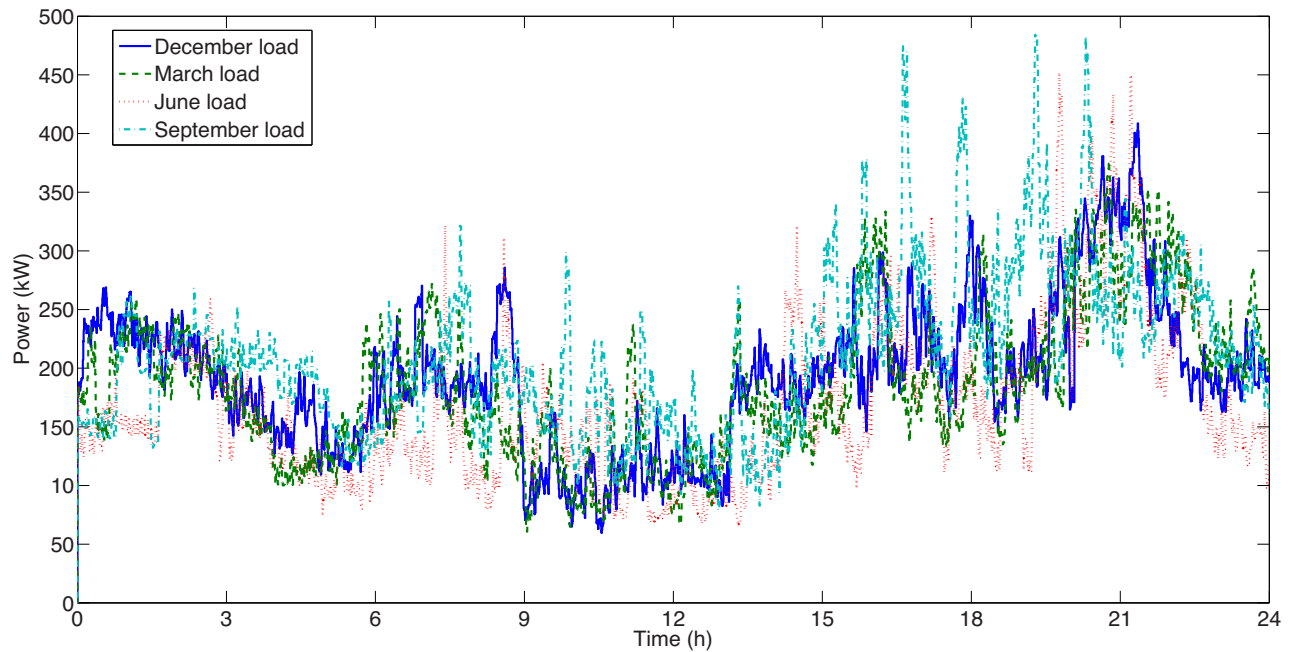
**Fig. 9.** 24 h load power profiles originating from measurements taken throughout the year at secondary substations. Measured data was sampled with 1 min resolution using KelVAtek data monitors/smart fuses [45].

efficiency during operation of the BESS. In these scenarios the SoC could float at 30%, 60%, 90% or 100%, and SoC maximum limits were 80%, 90% or 100%. In the cases examined the maximum SoC limit will also limit the floating SoC. Thus cases where the floating SoC would exceed the maximum SoC were excluded from the analysis. The minimum SoC varied from 0% to 20% depending on the scenario simulated. These combinations of floating SoC and SoC limits are chosen in a way that both the BESS power and energy delivered to the grid during discharge stays the same. Table 2 summarizes the above combinations.

Fig. 13 gathers the results of battery degradation for all the combinations examined. A most obvious remark is that floating at a higher SoC results in a higher rate of capacity loss. A factor of two increase in capacity loss can be noted for the two extreme cases i.e. floating at 100% and 30% SoC. This reflects the fact that we are here capturing only a single degradation mechanism i.e. accelerated SEI layer growth. Also, a non-linearity is observed in the rate by which battery degradation increases for higher values of floating SoC as shown in Fig. 13a for the first 10 h of operation. This is due to the non-linear potential of the graphite anode, which largely defines the rate of SEI layer growth. After the BESS begins to discharge the
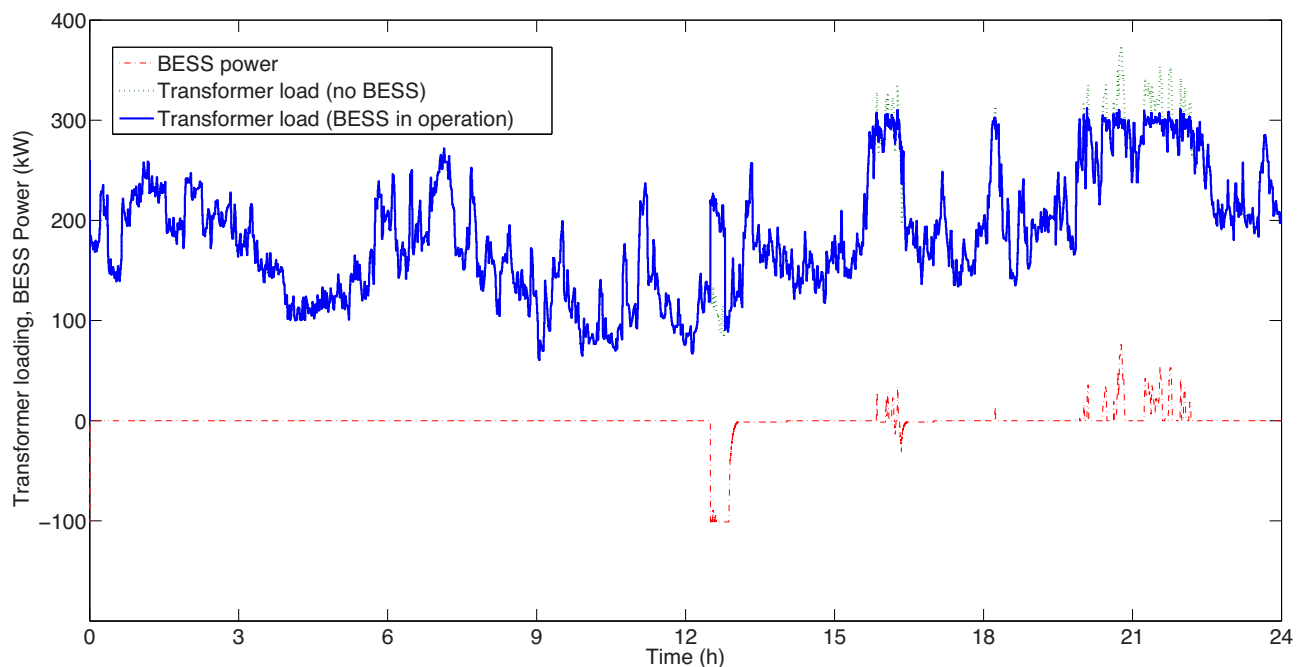


**Fig. 10.** Typical operation of the BESS, showing transformer loading and BESS power.

capacity loss will be different for each case depending on the SoC upper limit. Higher SoC limits will generally result in more time spent in higher SoC and consequently to greater capacity losses. Fig. 13b summarizes the results for degradation at the end of the examined 24 h period. Fig. 13b reaffirms that higher maximum SoC limits can result in greater capacity loss even if the chosen floating SoC was lower. It should be noted that the simulation of degradation was performed assuming an initially fresh cell and therefore capacity fade is expected to be faster in this initial period

until the SEI layer thickness builds up and limits the rate of film growth. Thus simulation extrapolation of the absolute degradation rate forward in time will not be linear, however the relative findings will still be valid.

Fig. 14 shows energy losses for the same combinations. It is evident that converter losses are not highly affected by the floating SoC but rather depend on the utilisation of the system. Fig. 14 reaffirms that for the cases examined the main contributor of losses in the BESS is the battery interface, and that higher $\Delta$SoC will
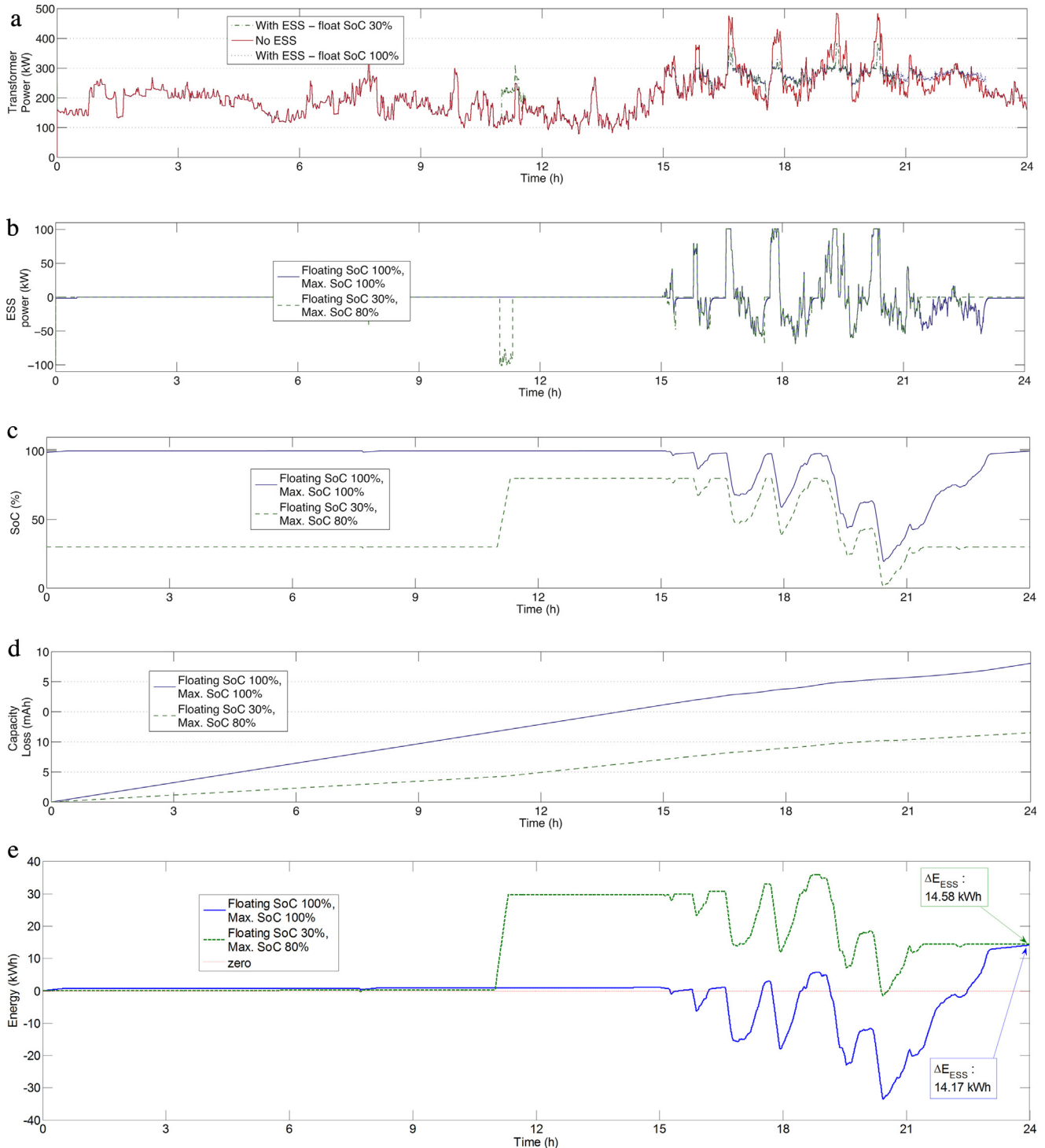


Fig. 11. BESS operation for two combinations of floating SoC and SoC limits, showing (a) Power flowing through the transformer (b) BESS power (c) battery SoC (d) Battery capacity loss and (e) energy absorbed and released during the operation of the BESS and the calculated roundtrip energy losses, $\Delta E_{ESS}$, over time for a 24 h cycle.

result in reduced battery efficiency, as shown for cases with lower floating SoC and SoC limits.

Based on the above observations it can be established that the choice of both the floating SoC and the SoC limits is critical in terms of round trip efficiency and degradation through battery capacity loss. Even though the same energy was delivered to the grid under the same power by several combinations, capacity loss was significantly different, depending on the load profile and the SoC restrictions imposed. Operating the battery at lower SoC will result in lower capacity loss, however, this would also imply that lower amounts of energy can be discharged to the grid and the related services might not be provided between specific times while

battery efficiency would also be reduced. In this analysis the authors have considered a single, albeit important, degradation mechanism, i.e. accelerated SEI layer growth, and are aware that operating at very low SoC will also introduce other degradation mechanisms.

The above conclusions suggest that an accurate load prediction could lead to optimised BESS operation where load demand can be met and capacity loss minimized. From this analysis it has been shown that any methodology used to meet simultaneously these two goals i.e. addressing a specific load demand and minimizing capacity loss, should account, at least, for both the chosen floating SoC and SoC limits.
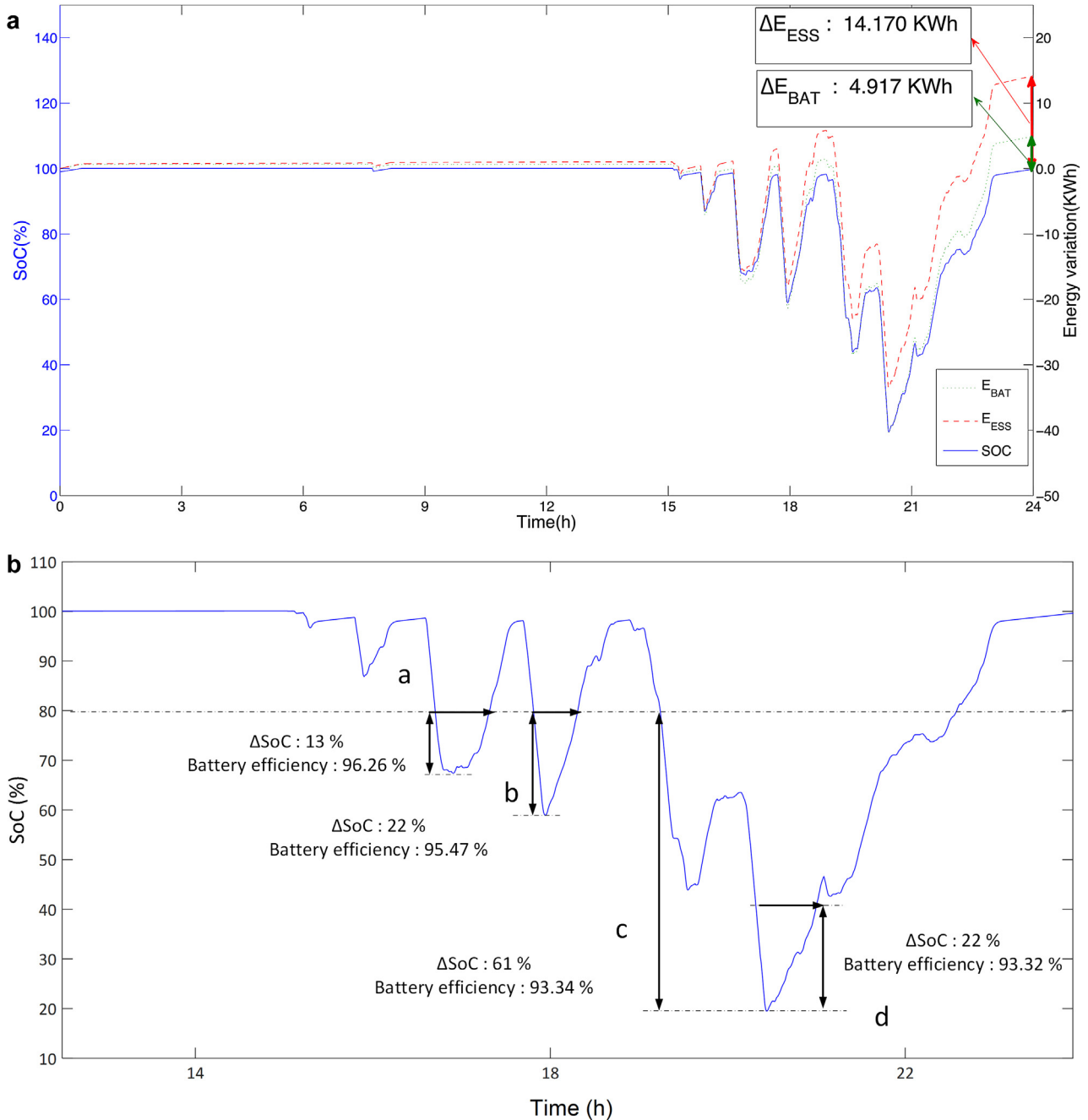


**Fig. 12.** Round trip energy losses and battery efficiency (a) Energy absorbed and released during the operation of the BESS, and the calculated total round trip energy losses, $\Delta E_{ESS}$, and battery round trip losses, $\Delta E_{bat}$, respectively, over time for a 24 h cycle (b) SoC over time for a 24 h cycle marking battery round-trip efficiency calculated for different $\Delta SoC$ and SoC values.

**Table 2**
Combinations of different floating SoC and SoC limits. V: valid combination X: non-valid combination.

| Float SoC (%) | Max.–Min. SoC (%) | | |
| --- | --- | --- | --- |
| | Max. 100–Min. 20 | Max. 90–Min. 10 | Max. 80–Min. 0 |
| 100 | V | X | X |
| 90 | V | V | X |
| 60 | V | V | V |
| 30 | V | V | V |

For the cases examined it was shown that roundtrip efficiency will strongly depend on the $\Delta$SoC. Operating at lower SoC and thus higher $\Delta$SoC will result in lower efficiencies due to higher battery polarisation losses. However, operating the battery at lower SoC reduces capacity losses due to higher anode potentials which largely define the rate of SEI layer growth. These two conclusions suggest that the targets of increasing roundtrip efficiency and minimizing battery degradation are contradictory in terms of
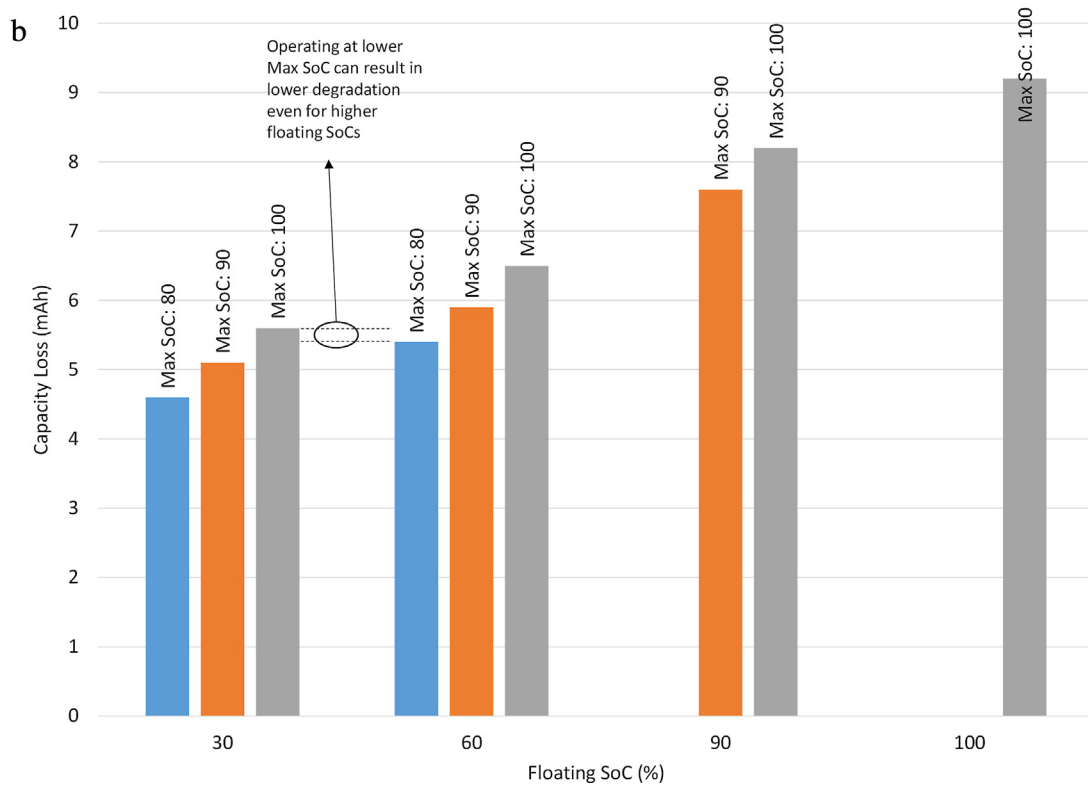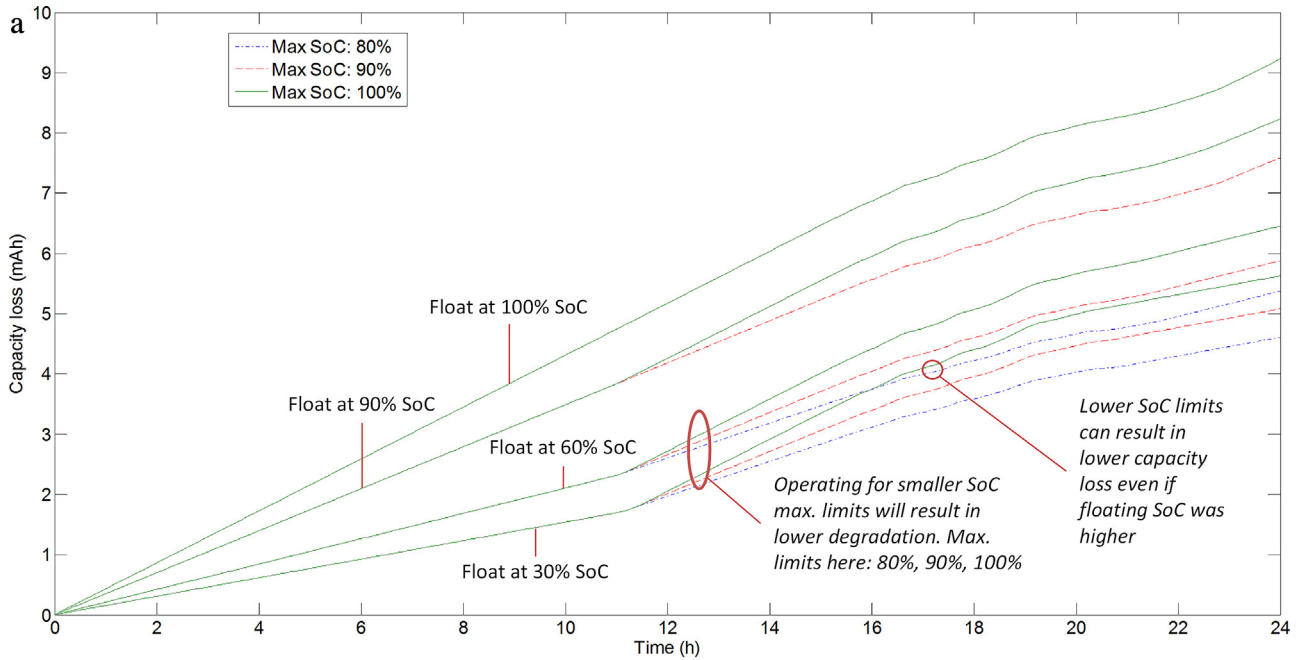


**Fig. 13.** Battery degradation for 24 h of operation for different combinations of floating SoC and maximum SoC limits (a) Capacity loss over time (b) total capacity loss at the end of the 24 h operation for a 4.8 Ah cell.
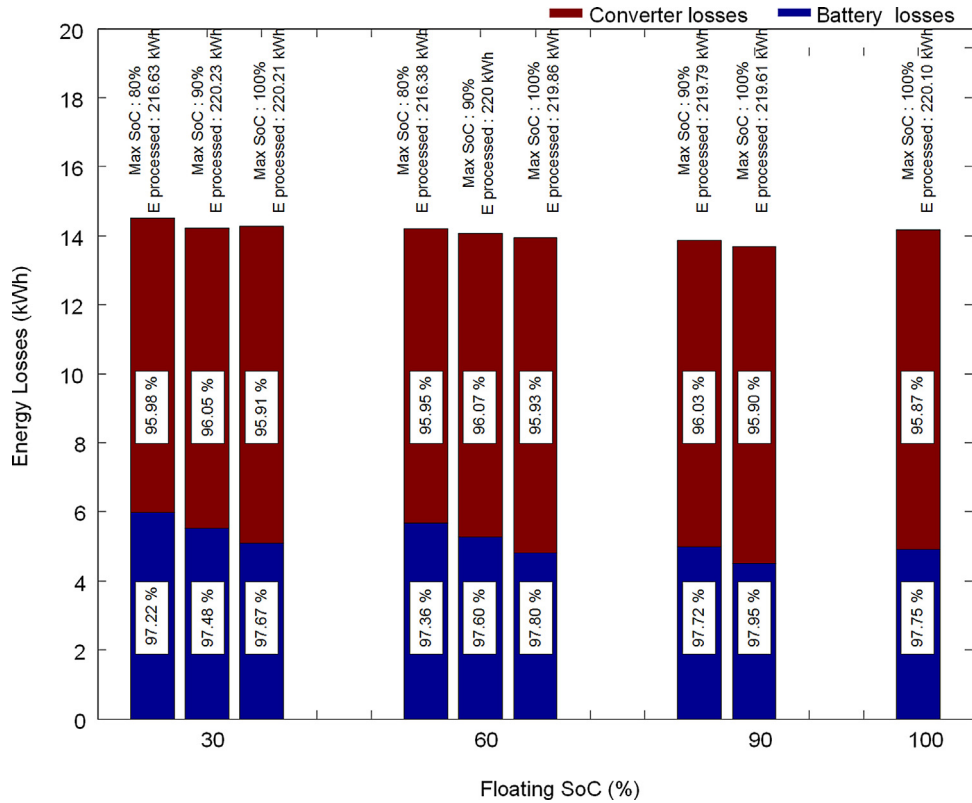
**Fig. 14.** Energy losses of the ESS as the sum of battery losses and converter losses. The efficiency of the converter and the battery is calculated based on the total energy processed during the day. Energy losses are presented for different combinations of floating SoC and maximum SoC limits.

establishing SoC set points, however these vary non-linearly and thus require models of sufficient fidelity to capture this.

## 4. Conclusions

Here we present an integrated modelling framework for a grid energy storage system, from battery to grid, and highlight the critical aspects in the development of a robust and fast model. Recorded simulation speed on an average desktop computer system was approximately 100 times faster than real time, which makes this model appropriate for simulating grid operation for timescales ranging from seconds up to a few days. The model incorporates accurate calculations of the key battery and power

converter properties that impose important constraints on the services provided to the grid. The latter can be taken into consideration in control algorithms targeting objectives that can range from voltage control to arbitrage and renewable energy time shift. This methodology could be applied to any other energy storage technology and thus acts as a platform for future work in this area.

The integrated model developed in this paper was used to simulate a typical load case in the UK on a network including distributed generation. An energy storage system was used to flatten transformer loading during evening periods of high demand. It was demonstrated that the same service can be delivered to the grid through a number of battery SoC set points,
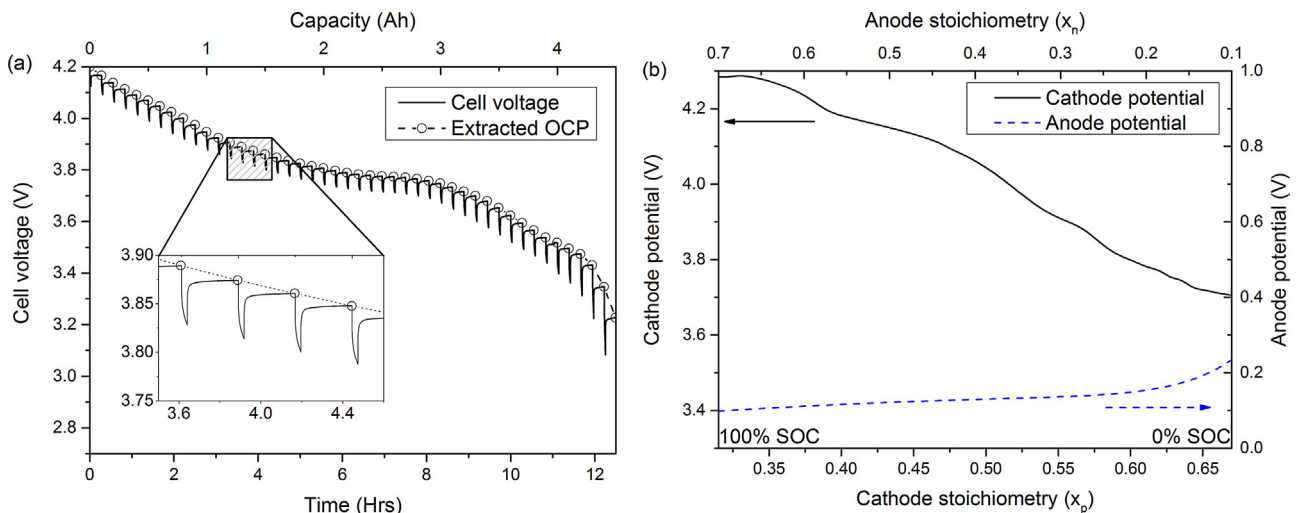


**Fig. 15.** (a) Cell voltage and OCP of a 4.8 Ah Kokam lithium–polymer battery under pulse discharge and (b) extracted OCP of the cathode and anode.

which are shown to result in significantly different values of battery degradation and round trip efficiency. Higher SoC floating points were shown to increase the rate of battery degradation, through accelerated SEI layer growth, whilst lower SoC floating points were shown to decrease system efficiency due to higher polarisation losses in the battery. This variation is non-linear due to the anode potential which largely governs the rate of SEI layer growth, this being the single degradation mechanism considered in this paper. Energy flow analysis also shows that, for the cases examined, the majority—59–67% of the system losses are originating from the power converter. This result combined with the decreased efficiency of the battery, as observed for the cases examined at lower SoC, raises the question whether a simpler converter topology such as the single stage converter [38] should be preferred given that the increase in converter efficiency could outweigh the limited SoC operational range and thus available capacity. Although such an investigation would exceed the scope of this paper, the proposed modelling approach can be used in order to quantify the monetary value of each converter interface based on the desired operation of the BESS.

These findings further support the importance of the integrated modelling approach as the results could be evaluated, either online or post processed, and used in conjunction with forecasting methodologies and actual costs of contracted services to optimise BESS operation i.e. to successfully meet grid control requirements in a cost-effective manner while increasing overall efficiency and battery lifetime.

## Acknowledgements

## Appendix A. Battery equations and parameters

*Battery equations and parameters*

| | | |
|---|---|---|
| $R_s^+$ | Radius of positive particle (m) | 8.5e-6 |
| $R_s^-$ | Radius of negative particle (m) | 12.5e-6 |
| $L^+$ | Cathode thickness (m) | 70e-6 |
| $L^-$ | Anode thickness (m) | 73.5e-6 |
| $c_e^0$ | Lithium-ion concentration in electrolyte (mol m$^{-3}$) | 1e3 |
| $\varepsilon^+$ | Cathode volume fraction | 0.5 |
| $\varepsilon^-$ | Anode volume fraction | 0.58 |
| $D^+$ | Cathode solid phase diffusion coefficient (m$^2$ s$^{-1}$) | 1.7e-14 |
| $D^-$ | Anode solid phase diffusion coefficient (m$^2$ s$^{-1}$) | 13e-14 |
| $x_{n,0}/x_{n,100}$ | Anode stoichiometry at 0% and 100% SoC | 0.1/0.7 |
| $x_{p,0}/x_{p,100}$ | Cathode stoichiometry at 0% and 100% SoC | 0.67/ 0.315 |
| $M_p$ | Molecular weight of the side reaction product (mol kg$^{-1}$) | 7.3e4 |
| $\rho_p$ | Density of side reaction product (kg m$^{-3}$) | 2.1e3 |
| $i_{0,s}$ | Exchange current density of side reaction (A m$^{-2}$) | 8e-8 |
| $\kappa_p$ | Conductivity of the side reaction product (S/m) | 1 |
| $E_{D_s^+}$ | Activation energy of cathode diffusion coefficient (J mol$^{-1}$) | 3.5e4 |
| $E_{D_s^+}$ | Activation energy of anode diffusion coefficient (J mol$^{-1}$) | 2.9e4 |
| $E_{i_{0,s}}$ | Activation energy of the side reaction (J mol$^{-1}$) | 3e4 |

*Battery parameter estimation*

The battery model was parameterised against test data for a 4.8 Ah lithium–polymer from Dow Kokam with an upper and lower voltage limit of 4.2 and 2.7 V. In order to extract the half-cell potential profiles for the anode and cathode, a fully charge cell was pulse discharged at 3.6 A for 100 s with a 900 s rest period. The cell voltage at the end of the rest period was taken as the OCP. This process was repeated until the voltage cut-offs were reached. The cathode half-cell potential profile was then acquired by comparison of the whole cell OCP and assuming the anode OCP to be the same as that presented by Ramadass et al. [33]. This is shown in Fig. 15.

## References

[1] ENSG. (2009). Electricity Networks Strategy Group: A Smart Grid Vision.
[2] G. Strbac, M. Aunedi, D. Pudjianto, P. Djapic, F. Teng, A. Sturt, et al., Strategic assessment of the role and value of energy storage systems in the UK low carbon energy future, Energy Futures Lab, Imperial College London, Report for Carbon Trust, published at https://workspace.imperial.ac.uk/ energyfutureslab/Public/Strategic%20Assessment%20of%20the%20Role% 20and%20Value%20of%20Energy%20Storage%20in%20the%20UK.pdf, (last accessed: November 2015) (2012).
[3] P.G. Taylor, R. Bolton, D. Stone, P. Upham, Developing pathways for energy storage in the UK using a coevolutionary framework, Energy Policy 63 (2013) 230–243.
[4] N.S. Pearre, L.G. Swan, Technoeconomic feasibility of grid storage: mapping electrical services and energy storage technologies, Appl. Energy 137 (2015) 501–510.
[5] N.S. Wade, P.C. Taylor, P.D. Lang, P.R. Jones, Evaluating the benefits of an electrical energy storage system in a future smart grid, Energy Policy 38 (2010) 7180–7188.
[6] N. Balta-Ozkan, T. Watson, P. Connor, C. Axon, L. Whitmarsh, R. Davidson, A. Spence, D. Xenias, L. Cipcigan, G. Taylor, Scenarios for the Development of Smart Grids in the UK - Synthesis Report (UKERC: London), published at https://ore.exeter.ac.uk/repository/bitstream/handle/10871/17720/Scenarios %20for%20the%20Development%20of%20Smart%20Grids%20in%20the%20UK %20Synthesis%20Report.pdf?sequence=2, (last accessed: November 2015) (2014).
[7] UK Power Networks, UKPN, (2014). Smarter Network Storage, Six Monthly Report.
[8] L. Sidebotham, (2014). Customer Led Network Revolution, Six Monthly Report.
[9] R.L. Fares, M.E. Webber, Combining a dynamic battery model with high-resolution smart grid data to assess microgrid islanding lifetime, Appl. Energy 137 (2015) 482–489.
[10] A. Purvins, M. Sumner, Optimal management of stationary lithium-ion battery system in electricity distribution grids, J. Power Sources 242 (2013) 742–755.
[11] R. Dufo-López, J.L. Bernal-Agustín, Techno-economic analysis of grid-connected battery storage, Energy Convers. Manage. 91 (2015) 394–404.
[12] D. Cottet, U. Drofenik, J.M. Meyer, A systematic design approach to thermal-electrical power electronics integration, Proc. Electron. Syst. Integr. Technol. Conf. (2008) 219–224.
[13] S.D. Pekarek, O. Wasynczuk, E.A. Walters, J.V. Jatskevich, C.E. Lucas, W. Ning, et al., An efficient multirate Simulation technique for power-electronic-based systems, IEEE Trans. Power Syst. 19 (2004) 399–409.
[14] T. Momma, M. Matsunaga, D. Mukoyama, T. Osaka, AC impedance analysis of lithium ion battery under temperature control, J. Power Sources 216 (2012) 304–307.
[15] D. Andre, M. Meiler, K. Steiner, H. Walz, T. Soczka-Guth, D.U. Sauer, Characterization of high-power lithium-ion batteries by electrochemical impedance spectroscopy II: modelling, J. Power Sources 196 (2011) 5349–5356.
[16] J. Xu, C.C. Mi, B. Cao, J. Cao, A new method to estimate the state of charge of lithium-ion batteries based on the battery impedance model, J. Power Sources 233 (2013) 277–284.
[17] W. Waag, S. Käbitz, D.U. Sauer, Experimental investigation of the lithium-ion battery impedance characteristic at various conditions and aging states and its influence on the application, Appl. Energy 102 (2013) 885–897.
[18] Z. Pan, W. Jiangfeng, D. Yiping, Capacity allocation of a hybrid energy storage system for power system peak shaving at high wind power penetration level, Renew. Energ. 75 (2015) 541–549.
[19] M.D. Arifujjaman, A comprehensive power loss, efficiency, reliability and cost calculation of a 1 MW/500 kWh battery based energy storage system for frequency regulation application, Renew. Energ. 74 (2015) 158–169.
[20] L. Sigrist, E. Lobato, L. Rouco, Energy storage systems providing primary reserve and peak shaving in small isolated power systems: an economic assessment, Int. J. Electr. Power Energy Syst. 53 (2013) 675–683.
[21] L. Johnston, F. Díaz-González, O. Gomis-Bellmunt, C. Corchero-García, M. Cruz-Zambrano, Methodology for the economic optimisation of energy storage

systems for frequency support in wind power plants, Appl. Energy 137 (2015) 660–669.

[22] I.S. Gkavanoudis, S.C. Demoulias, A combined fault ride-through and power smoothing control method for full-converter wind turbines employing supercapacitor energy storage system, Electric Power Syst. Res. 106 (2014) 62–72.

[23] B. Ge, W. Wang, D. Bi, C.B. Rogers, F.Z. Peng, T.A. de Almeida, Abu-Rub Haitham, Energy storage system-based power control for grid-connected wind power farm, Int. J. Electrical Power Energy Syst. 44 (2013) 115–122.

[24] Y. Luo, L. Shi, G. Tu, Optimal sizing and control strategy of isolated grid with wind power and energy storage system, Energy Convers. Manage. 80 (2014) 407–415.

[25] R.E. Gerver, J.P. Meyers, Three-dimensional modeling of electrochemical performance and heat generation of lithium-ion batteries in tabbed planar configurations, J. Electrochem. Soc. 158 (2011) A835.

[26] M. Guo, G.-H. Kim, R.E. White, A three-dimensional multi-physics model for a Li-ion battery, J. Power Sources 240 (2013) 80–94.

[27] G.G. Botte, V.R. Subramanian, R.E. White, Mathematical modeling of secondary lithium batteries, Electrochim. Acta 45 (2000) 2595–2609.

[28] D.W. Dees, V.S. Battaglia, A. Bélanger, Electrochemical modeling of lithium polymer batteries, J. Power Sources 110 (2002) 310–320.

[29] K. Smith, C.-Y. Wang, Power and thermal characterization of a lithium-ion battery pack for hybrid-electric vehicles, J. Power Sources 160 (2006) 662–673.

[30] B. Wu, V. Yufit, M. Marinescu, G.J. Offer, R.F. Martinez-Botas, N.P. Brandon, Coupled thermal-electrochemical modelling of uneven heat generation in lithium-ion battery packs, J. Power Sources 243 (2013) 544–554.

[31] S. Santhanagopalan, R.E. White, Online estimation of the state of charge of a lithium ion cell, J. Power Sources 161 (2006) 1346–1355.

[32] J. Vetter, P. Novák, M.R. Wagner, C. Veit, K.-C. Möller, J.O. Besenhard, et al., Ageing mechanisms in lithium-ion batteries, J. Power Sources 147 (2005) 269–281.

[33] P. Ramadass, B. Haran, P.M. Gomadam, R. White, B.N. Popov, Development of first principles capacity fade model for Li-ion cells, J. Electrochem. Soc. 151 (2004) A196.

[34] Y. Troxler, B. Wu, M. Marinescu, V. Yufit, Y. Patel, A.J. Marquis, et al., The effect of thermal gradients on the performance of lithium-ion batteries, J. Power Sources (2013) 1–8.

[35] N. Chaturvedi, R. Klein, Algorithms for advanced battery-management systems, Control Syst. (2010) 49–68.

[36] B. Wu, V. Yufit, Y. Merla, R.F. Martinez-Botas, N.P. Brandon, G.J. Offer, Differential thermal voltammetry for tracking of degradation in lithium-ion batteries, J. Power Sources 273 (2015) 495–501.

[37] I. Trintis, S. Munk-Nielsen, R. Teodorescu, Single Stage Grid Converters for Battery Energy Storage in Power Electronics, Proc. 5th IET International Conference on Machines and Drives (PEMD 2010), 2010, pp. 1–6.

[38] S. Ponnaluri, G.O. Linhofer, J.K. Steinke, P.K. Steimer, Comparison of Single and Two Stage Topologies for Interface of Bess or Fuel Cell System Using the Abb Standard Power Electronics Building Blocks, Proc. 2005 European Conference on Power Electronics and Applications, 2005, pp. 9.

[39] G. Kalcon, G.P. Adam, O. Anaya-Lara, G. Burt, K.L. Lo, Analytical efficiency evaluation of two and three level VSC-HVDC transmission links, Int. J. Electrical Power Energy Syst. 44 (2013) 1–6.

[40] Z. Zhou, M.S. Khanniche, P. Igic, S.T. Kong, M. Towers, P.A. Mawby, A Fast Power Loss Calculation Method for Long Real Time Thermal Simulation of Igbt Modules for a Three-phase Inverter System, Proc. 2005 European Conference on Power Electronics and Applications, 2005, pp. 9–10.

[41] R.B. Bodapati, A. Sarma, Losses Calculation of PWM Inverter, National Conference in Mechanical Engineering Research and Postgraduate Students (1st NCMER 2010), 2010, pp. 159–174.

[42] U. Drofenik, J.W. Kolar, A General Scheme for Calculating Switching-and Conduction-losses of Power Semiconductors in Numerical Circuit Simulations of Power Electronic Systems, Proc. 2005 International Power Electronics Conference (IPEC'05), 2005, pp. 4–8.

[43] A.D. Rajapakse, A.M. Gole, P.L. Wilson, Electromagnetic transients simulation models for accurate representation of switching losses and thermal performance in power electronic systems, IEEE Trans. Power Deliv. 20 (2005) 319–327.

[44] ABB. Datasheet of low voltage transformers—Three phase power transformer published at https://library.e.abb.com/public/ b0267a3c7df1cb12c1257c7100427f5d/1LES100025-ZD-Low-Voltage-Transformers.pdf, last accessed: June 2015.

[45] Low Carbon Network Fund Project, ENWT1001—The Smart Fuse, Closedown Report, May 2014. http://www.enwl.co.uk/docs/default-source/future-documents/project-closedown-report.pdf?sfvrsn=0, last accessed: June 2015.